Flow Characteristics of Ore Slurry Injection Process in the Intermediate Warehouse of Deep-sea Ore Hydraulic Transmission

W. Chen[1,2,3†], H. L. Xu[1,3], B. Wu[1,3], D. Hu[2], S. Wang[2] and P. Lin[2]

[1] *School of Mechanical and Electrical Engineering, Central South University, Changsha, Hunan, 410083, China*
[2] *Department of Energy and Electrical Engineering, Hunan University of Humanities, Science and Technology, Loudi, Hunan 417000, China*
[3] *State Key Laboratory of High-Performance Complex Manufacturing, Changsha, Hunan 410083, China*

†*Corresponding Author Email: 3187@huhst.edu.cn*

ABSTRACT

This study proposes a new intermediate warehouse to prevent the problem that the ore in the vertical pipeline hydraulic lifting system blocks the nozzle during the process of being sucked into the lifting hard tube. A mathematical model and a finite element model of ore transport are established. Numerical simulation and experimental research are performed on the process of ore injection into the intermediate warehouse. Results show that the proposed intermediate warehouse has higher ore transmission efficiency, smaller pressure pulsation, and more stable transmission process compared with the traditional structure scheme. The larger the slurry conveying flow, the shorter the time required to convey the ore. In the process of slurry injection, the closer to the inlet, the more uneven the velocity distribution on the Z section, and the more concentrated the dynamic pressure. The closer to the lower end of the intermediate warehouse, the more dispersed the dynamic pressure, and the fluctuation of dynamic pressure in the intermediate warehouse is the main cause of unstable flow. The feed flow has a great influence on the stress state of the intermediate warehouse structure, the ore transfer time, and the stress decay period. The feed flow rate should be reasonably selected to meet the working requirements.

Keywords: Deep-sea mining; Intermediate warehouse; Ore transfer; Numerical simulation; Flow characteristics.
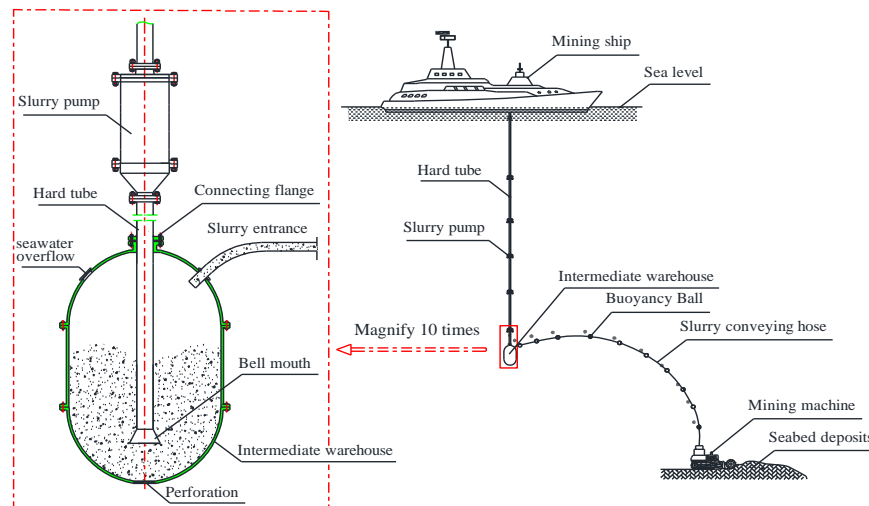
NOMENCLATURE

F_l	external force per unit mass of the liquid phase	u_l	liquid phase velocity vector
F_s	solid phase the external force per unit mass of the phase	u_s	solid phase velocity vector
M_l	interphase force acting on the liquid phase	t	time
		ρ_s	solid phase density
M_s	interphase force acting on the solid phase	τ_l	stress tensor of the liquid phase
P	equivalent stress	τ_s	stress tensor experienced by the solid phase
u	velocity vector	φ_V	solid phase volume concentration

1. INTRODUCTION

Deep-sea mining technology is a complex systems, it mainly includes mining machine, water surface support system, control system and ore transfer system. (Cheng *et al*. 2013, Dasheng *et al*. 2015). In accordance with different working principles, the ore transfer system is mainly divided into a trailer mining system, a continuous rope bucket mining system, a shuttle mining system, and a fluid lifting mining system (Felippa and Chung 1981). Among them, the fluid lifting mining system is considered to be the most promising mining method for commercial applications (Gazis *et al*. 2018).

Fig. 1 Structure of the intermediate warehouse of the hydraulic lifting system of the slurry pump.

In accordance with different ore hard tube lines and equipment, the fluid lifting mining method is mainly divided into clean water pump lifting method and slurry pump lifting method (Grebe 1997). As the current mainstream technology of deep-sea mining, the slurry pump lifting method has the characteristics of large lift, large flow, and high efficiency, and is extremely popular in the field of mining engineering worldwide. Although this method has many advantages, it still has the problem of easy accumulation of minerals at the entrance of the ore lifting system and nozzle clogging in actual mining (Hailiang 2008, Hailiang *et al*. 2020, Hai-Liang *et al*. 2019).

In order to solve the phenomenon that the ore is easy to plug the nozzle, the project team invented the "intermediate warehouse of ore hydraulic lifting system". Its basic structure is shown in Fig. 1.

Its working principle is as follows: the mining machine collects the polymetallic nodules and crushes them, they are transported to the intermediate warehouse by the pulp conveying hose. Under the action of the slurry pump, a vertical upward water jet is formed because of negative pressure between the bell mouth suction port of the hard tube and the intermediate warehouse. The submerged water jet has an entrainment effect on the surrounding fluid and disturbs the ore particles settled at the bottom of the intermediate warehouse to produce vibration. Ore particles are transported to the mining ship under the jet water hammer and the suction power of the slurry pump.

The ore transmission process of the slurry pump hydraulic lifting system mainly includes two parts: (1) The ore is injected into the intermediate warehouse by the slurry conveying hose. (2) The lifting process of ore in a vertical pipeline.

This study analyzes the process of ore injection into the intermediate warehouse to improve the working efficiency of the transmission process. The motion law and pressure distribution of the two-phase fluid in the intermediate warehouse and the fluid-structure

coupling analysis during the slurry injection process are studied when the ore conveying equipment is in different working parameters.
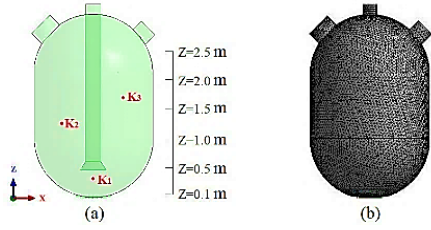
2. MODEL ANALYSIS

The initial parameters of the ore hydraulic transmission system are mainly based on the technical design research report of the China Oceanic Association's "Tenth Five-Year Plan" mining pilot system (Hoffmann 1995). Its main technical parameters are shown in Table 1.

Table 1 Technical indicators and parameters of ore transportation system

Technical index	Parameter value	Unit
Mineral sea depth (h)	6000	m
Working depth of ore transportation equipment (L)	5400	m
Extreme wind velocity	16	m/s
Average wind velocity	8	m/s
Average wave height	2.5	m
Sea surface velocity	1.7	m/s
Ocean current velocity	0.01~0.1	m/s
Sea temperature	22.0~30.2	℃
Sea water density	1052	kg/m^3
Intermediate warehouse volume	28	m^3
Ore collection capacity	45	t/h
Water content of polymetallic nodules	33.3%	-
Conveying ore concentration	6~20%	-
Pipe inner diameter	300	mm
Polymetallic nodules diameter (d)	10~40	mm
Polymetallic nodules density	2040	kg/m^3
Particle settling velocity	0.62	m/s

2.1 Geometric Model and Meshing

A geometric model of the intermediate warehouse was established to study the flow distribution characteristics of the slurry injection process in the intermediate warehouse, as shown in Fig. 2(a).

Fig. 2. Intermediate warehouse model. (a) Geometric model (perspective view), (b) Computational domain mesh model.

The physical calculation model of the internal flow field in the intermediate warehouse of the ore conveying equipment must be determined and established, and the calculation model should be discretized before the numerical simulation. The fluid domain mesh model of the intermediate tank is shown in Fig. 2(b).

2.2 Physical Parameters and Boundary Conditions

2.2.1 Basic assumptions

To ensure the feasibility of the calculation and the reliability of the calculation results, this article makes the following assumptions.

(1) The flow field is stable, and no temperature difference is observed.

(2) Regardless of the influence of shape, the maximum filling volume fraction of the ore accumulation layer is 0.6.

(3) The collision between particles is ignored, but a two-phase coupling is found between seawater and particles.

(4) Regardless of the effect of particle deposition on the wall, the mass of particles in the pipeline is conserved.

2.2.2 Governing Equation

In the computing environment of unsteady flow, ignoring the surface tension of the fluid, and assuming that the mixed fluid is an incompressible viscous fluid, the equation for calculating the flow field can be expressed as follows (Xu *et al.* 2012):

(1) Momentum equation

Liquid phase momentum equation

$$\frac{\partial}{\partial t}\left[(1-\varphi)u_l\right]+\nabla\cdot\left[(1-\varphi)u_l\right]=(1-\varphi)F_l-\frac{1}{\rho_l}\nabla\cdot\left[(1-\varphi)P\right]$$
$$+\frac{1}{\rho_l}\nabla\cdot\left[(1-\varphi)\tau_l\right]+\frac{M_l}{\rho_l} \quad (1)$$

Solid phase momentum equation

$$\frac{\partial}{\partial t}\left[\varphi u_s\right]+\nabla\cdot\left(\varphi u_s\right)=\varphi F_s-\frac{1}{\rho_s}\nabla\cdot\left(\varphi P\right)+\frac{1}{\rho_s}\nabla\cdot\left(\varphi \tau_s\right)+\frac{M_s}{\rho_s} \quad (2)$$

(2) Continuous phase equation

Liquid phase continuous equation

$$\frac{\partial(1-\varphi)}{\partial t}+\frac{\partial\left[(1-\varphi)u_{le}\right]}{\partial x_e}=0 \quad (3)$$

where the subscript *l* represents the liquid phase, and the subscript *e* represents the tensor index, $e = 1,2,3$.

Solid phase continuous equation

$$\frac{\partial\varphi}{\partial t}+\frac{\partial\varphi u_{se}}{\partial x_e}=0 \quad (4)$$

where the subscript *s* represents the solid phase.

2.3 Physical Parameters and Boundary Conditions

Because the limit sea depth of the mining area is about 6000 m, the environmental pressure of the calculation model is set to 60 MPa. The main phase is seawater, the secondary phase is solid particles of polymetallic nodules.

The inlet conditions, outlet conditions, and other boundaries of the calculation domain must be consistent with the actual operating conditions to improve the validity and reliability of the calculation results. The specific settings are as follows:

(1) Inlet conditions: Define the inlet boundary as the velocity inlet, set the flow velocity direction of the solid-liquid two-phase flow perpendicular to the inlet surface of the pulp inlet.

(2) Exit conditions: The ore particles are deposited in the intermediate warehouse after the slurry is injected into the intermediate warehouse, and the seawater in the intermediate warehouse flows to the external marine environment through the seawater overflow port, so the seawater overflow port is defined as outflow boundary.

(3) Solid wall boundary: Except for the inlet and outlet of the computational domain boundary of the intermediate warehouse, other boundaries are defined as no-slip wall boundary conditions.

3. MODEL VALIDATION

The rated volume flow (*Q*) of the slurry pump is 220 m^3/h, and the adjusted feed flow is 180, 220, 260, and 300 m^3/h. The flow process, velocity distribution, and pressure distribution of the flow field in the intermediate warehouse are studied under different volume flow.
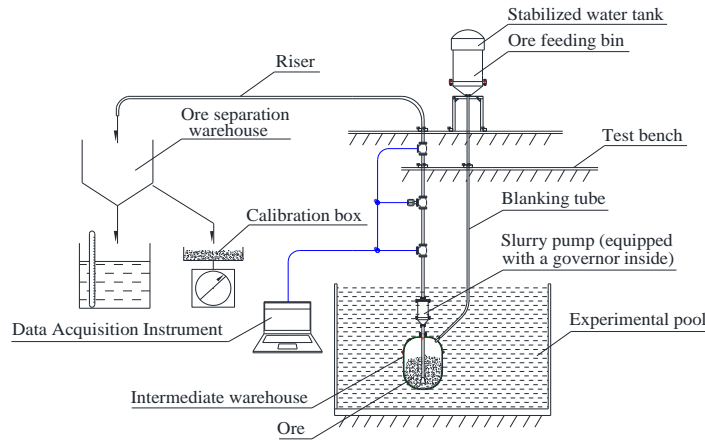
To fully analyze the flow characteristics in the intermediate warehouse, this study selects different Z cross sections on the symmetrical plane of the intermediate warehouse (*Y*=0 m section) as the research points. The positions of the different Z section is shown in Fig. 2(a).

3.1 Experimental Study

Laboratory testing was performed on scaled deep-sea mining system models to study the ore flow characteristics in the intermediate warehouse. The ratio of the model to the real object is 1: 5.

3.1.1 Model design based on similarity laws

The experimental model and the object model must have a certain proportional relationship in the corresponding physical quantities to make the

Fig. 3. Schematic of the experimental system structure.

movement of the model show the main phenomenon and performance of the real object (Yang *et al.* 2011). The main similarity scales mainly include geometric, motion, and dynamic similarities. The similar scale must satisfy the following relationships.

$$\left.\begin{array}{l} \delta_v^{\,2} = \delta_l \cdot \delta_g \\ \delta_p = \delta_\rho \cdot \delta_v^{\,2} \\ \delta_\lambda = \delta_l \cdot \delta_v \end{array}\right\} \tag{5}$$

where δ_v is the speed scale, δ_l is the linear scale, δ_p is the pressure (stress) scale, δ_ρ is the mass scale, and δ_λ is the kinematic viscosity scale. The gravitational acceleration scale δ_g=1 because the model and prototype have the same gravitational field. From the abovementioned proportional relationship, other proportional relationships can be derived on the basis of similar principles, as shown in Table 2.

Table 2 Motion similarity and power similarity scale

Motion similar scale		Power-similar scale	
Scale	v / v'	Scale	Expression
Speed scale (δ_v)	δ_l / δ_v	Density scale (δ_ρ)	ρ / ρ'
Time scale (δ_t)	δ_v^2 / δ_l	Mass scale (δ_m)	$\delta_\rho \delta_l^3$
Acceleration scale (δ_a)	$\delta_l^2 \delta_v$	Force scale (δ_F)	$\delta_\rho \delta_l^2 \delta_v^2$
Flow scale (δ_q)	$\delta_l \delta_v$	Moment scale (δ_M)	$\delta_\rho \delta_l^3 \delta_v^2$
Kinematic viscosity scale (δ_υ)	δ_v / δ_l	Pressure (stress) scale (δ_p)	$\delta_\rho \delta_v^2$
Angular velocity scale (δ_ω)	v / v'	Dynamic viscosity scale (δ_μ)	$\delta_\rho \delta_l \delta_v$

In accordance with the model making ability and experimental conditions, a geometric similar model with a scale of 1 : 5 is adopted, that is, δ_l=5. The speed scale is set to δ_v=1, and the volume flow scale is set to δ_q=25. In accordance with the abovementioned similar scale, the size of the similar model is determined as follows.

Table 3 Prototype and model parameter formulation

Physical parameter	Similar scale	Prototype	Model
Inner diameter of the intermediate warehouse（mm）	$\delta_l = 5$	1880	376
Volume of the intermediate warehouse（m³）	$\delta_l = 5$	6	0.47
Inner diameter of hard tube（mm）	$\delta_l = 5$	200	40
Ore particle diameter（mm）	$\delta_l = 5$	30	6
Average density of fluid（kg/m³）	$\delta_\rho = 0.971$	1126.5	1160
Feed flow（m³/h）	$\delta_q = 32$	250	7.81

3.1.2 Experimental Program

The deep-sea ore conveying equipment should work underwater to make the experiment process closer to the real situation. Thus, the deep-sea ore conveying equipment is installed in the water tank. The structure of the experimental system is shown in Fig. 3.

During the experiment, the water tank is filled with water, the valve is opened, and the slurry pump is started. The governor is adjusted after a stable water flow is observed at the outlet of the pipeline to stabilize the final speed of the slurry pump at the required working condition. The ore feeding bin valve is opened to feed the nodule particles with a predetermined concentration. When the system runs stably, the stabilized water tank is opened, and the mixed slurry enters the ore separation warehouse. The volume concentration of the solid phase is calculated by weighing the amount of nodules in the ore separation warehouse. The working flow is calculated by the time it takes to fill the calibration box.

3.2 Analysis of Experimental Results

Under different feeding parameters (different flow rates, different concentrations, and different ore

particle sizes), the feeding time when the ore feeding volume in the intermediate warehouse reaches 0.6 is taken as the evaluation index. The differences between the experimental test results and the numerical calculation results were compared and analyzed to verify the accuracy of the numerical model and numerical method.

Use univariate analysis in experimental research to reduce experimental sample size. The experimental results are shown in Tables 4, 5, and 6. Comparing the experimental measurement results with the numerical calculation results, it can be seen that the change trend is the same, and the errors are both within 5%. The experimental results verify the numerical model well, and the main reasons for the errors are as follows:

(1) Calculation errors caused by assumptions in the calculation conditions (for example, assuming that the ore particles are spherical, and no collision and energy exchange occur during the flow) and the simplification of the calculation model.

(2) System error due to experimental test equipment, such as flowmeter error, valve leakage error, and error caused by the vibration of the experimental system.

Table 4 Comparison of experimental and simulation results under different feed flows

| Feed flow (m³/h) | Feeding time (s) | | Error (%) |
	Experimental measurement results	Results of numerical simulation	
180	609	620	1.77
220	557	570	2.28
260	504	520	3.08
300	445	460	3.26

Table 5 Comparison of experimental and simulation results at different particle concentrations

| Particle concentrat-ion (%) | Feeding time (s) | | Error (%) |
	Experimental measurement results	Results of numerical simulation	
5	641	652	1.69
8	603	614	1.79
10	557	570	2.28
15	488	504	3.17

Table 6 Comparison of experimental and simulation results under different particle sizes

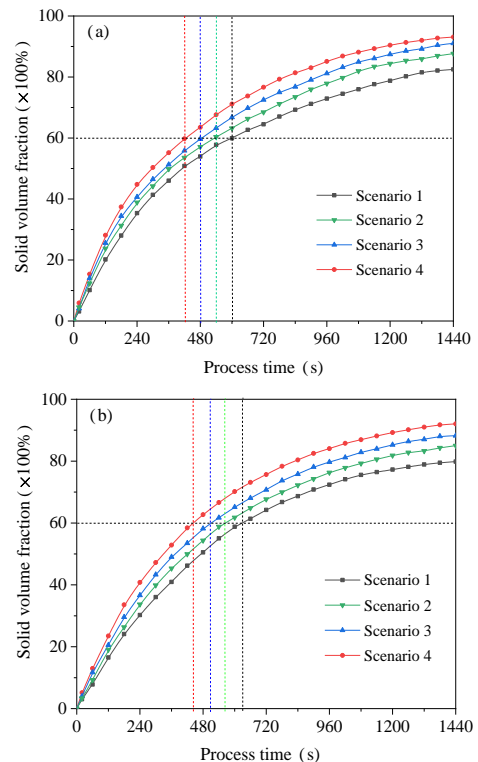| Particle size (mm) | Feeding time (s) | | Error (%) |
	Experimental measurement results	Results of numerical simulation	
10	557	570	2.28
20	521	535	2.62
30	484	502	3.59
40	448	467	4.07

4 RESULT ANALYSIS AND DISCUSSION

4.1 Variation Law of Ore Volume Fraction in the Intermediate Warehouse with Process Time

This section first analyzes the variation law of ore with process time during the slurry injection process in the intermediate warehouse before studying the flow conditions and pressure distribution characteristics of the solid and liquid phases in the intermediate warehouse. The specific research parameters are shown in Table 7.

Table 7 Calculation parameters of the change law of ore with process time in the process of slurry injection

Scheme serial number	Slurry conveying flow （m³/h）	Slurry conveying concentration （%）	Ore particle size (mm)
Scheme 1	180	10	20
Scheme 2	220	10	20
Scheme 3	260	10	20
Scheme 4	300	10	20

Figure 4 shows the calculation results of the change law of ore with process time during the slurry injection process in the intermediate warehouse. Fig. 4(a) shows the calculation result of the technical scheme adopted in this study (hereinafter referred to as the new scheme). Figure 4(b) shows the calculation results when using the conventional scheme (hereinafter referred to as the general scheme).
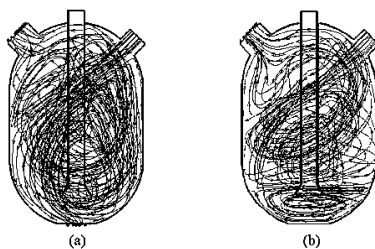

Fig. 4. Variation curve of ore particle volume fraction in the intermediate warehouse with process time.

The calculation results in Fig. 4(a) show that the volume of ore particles in the intermediate warehouse increases with the increase in the process time. The increase in the initial time is greater than that in the second half. The main reason is that with the accumulation of ore in the intermediate warehouse, the dynamic pressure and turbulent kinetic energy in the intermediate warehouse in the second half time are obvious compared with the initial stage of feeding. Enhancement increases the resistance of the pulp inlet, making the feeding rate slower.

The calculation results show that the larger the slurry conveying flow rate, the shorter the time required for the volume of the ore particles to reach the target value (60%). When the slurry transport concentration is 10%, the ore particle size is 20 mm. The flow rates are 180, 220, 260, and 300 m^3/h, and the times required for the ore volume to reach 60% are 600, 540, 480, and 440 s, respectively.

Compared with the calculated results in Fig. 4(b) (conventional scheme), the feeding time required for the new scheme is significantly reduced. Specifically, the feeding efficiency of the new scheme is higher than that of the traditional scheme in the first half of the feeding cycle. This condition is because increasing the injection hole at the bottom is equivalent to adding a pressure relief port in the intermediate warehouse. During the ore feeding process, the back pressure in the intermediate warehouse is slightly reduced, making the feeding process smoother.

However, the difference in feeding rate between the new scheme and the traditional scheme is reduced when entering the second half of the cycle. The advantage of the new scheme is weakened. This condition is because after the ore is accumulated to a certain extent, the part of the ore settled at the bottom of the intermediate warehouse will block the injection hole, which will increase the turbulent kinetic energy in the intermediate warehouse and reduce the feeding efficiency.

Fig. 5. Flow traces during slurry injection.

Figure 5 shows the flow trace diagram during the slurry injection process in the intermediate warehouse. Figure 5(a) displays the calculation result of the new scheme, and Fig. 5(b) indicates the calculation result of the conventional scheme.

The calculation results in Fig. 5(a) show that the solid–liquid two-phase flow begins to separate after the slurry flows into the intermediate warehouse. A part of the seawater flows out of the intermediate warehouse through the seawater overflow in the direction of the incoming flow. Another part of the mixed fluid with higher particle concentration and larger specific gravity is deposited to the bottom of the intermediate warehouse.

The calculation results in Fig. 5(b) show that the slurry forms a large-scale radial circulation in the intermediate warehouse after the submerged jet enters the intermediate warehouse. It pushes the liquid phase water out of the intermediate warehouse from the overflow port on the upper left. The separation efficiency of the solid phase and the liquid phase in the pulp is affected because of the long moving distance and high energy consumption, resulting in a decrease in the feeding efficiency.
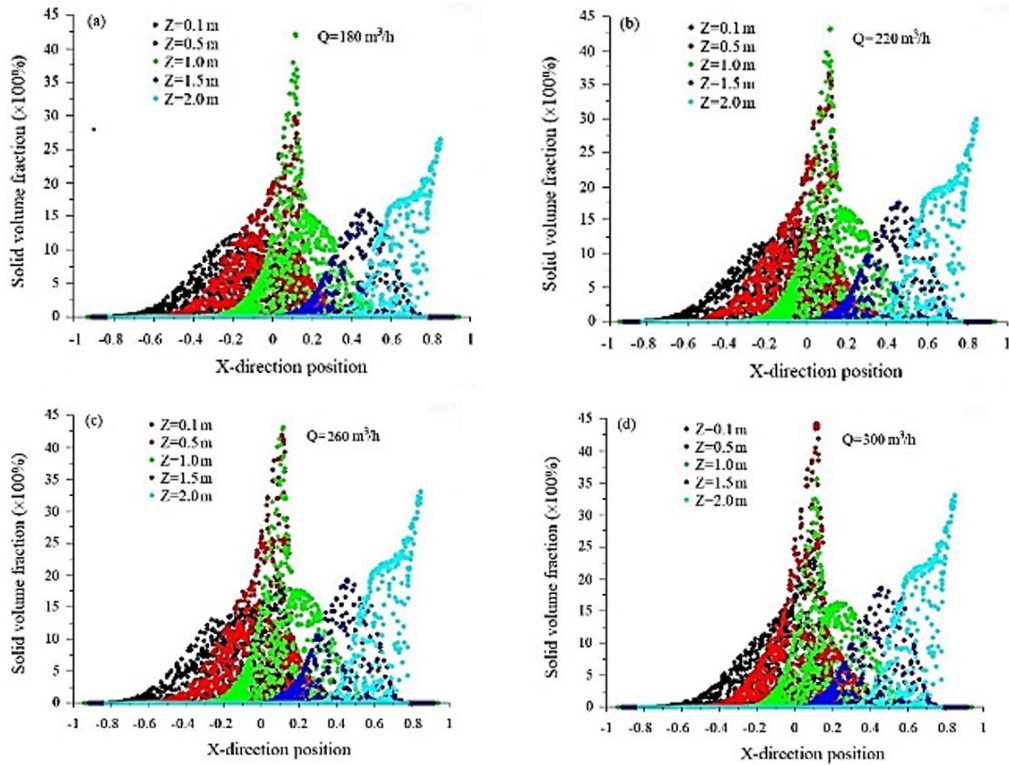
Figure 6 shows the ore concentration distribution on different Z sections under different feed flow rates. The ore concentration increases with the increase in the feed flow rate on the same Z section. The closer to the bottom of the intermediate warehouse, the greater the effect of the feed flow on its concentration distribution. The larger the feed flow rate, the ore concentration distribution tends to shift to the left side of the intermediate warehouse. This condition is because the kinetic energy obtained by the ore particles is larger when the flow rate is larger, which increases its lateral displacement in the intermediate warehouse.

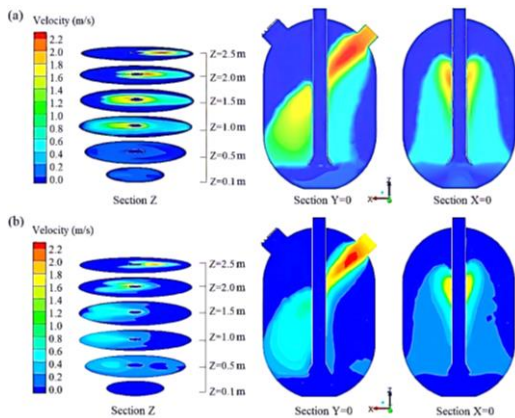**4.2 Distribution Law of Velocity Field**

Figure 7 shows the distribution cloud map of velocity (absolute velocity value) at different sections in the intermediate warehouse. Figure 7(a) displays the calculation result of the new scheme, and Fig. 7(b) indicates the calculation result of the conventional scheme.

The calculation results in Fig. 7 show that when the core section of the jet extends to the position of the lift tube in the intermediate warehouse, it collides with the wall of the lift tube after the slurry is injected into the intermediate warehouse through the slurry inlet, resulting in energy loss, and the flow velocity decreases sharply. However, most of the fluids can still bypass the hard tube wall and flow to the left area of the intermediate warehouse. After the other part of the fluid is blocked by the pipe wall of the lifting hard tube, it makes a short local circulation on the right side of the pipe wall of the lifting hard tube, and then makes a stable settlement movement in the intermediate warehouse.

The velocity distribution of the Z-direction section in Figure 7 shows that the mixed fluid gradually spreads from the center to the surrounding of the wall of the intermediate warehouse during the slurry injection process. Uneven velocity distribution is observed. The closer to the entrance, the more uneven the velocity distribution on the Z section. The fluid velocity in the middle region is significantly higher than that of the peripheral fluid. This condition is because when the slurry is injected into the intermediate warehouse in the form of a submerged jet, the jet impacts and entrains the

Fig. 6. Ore concentration distribution on different sections.

Fig. 7. Velocity distribution cloud map at different sections.

original liquid phase water in the intermediate warehouse at the cross section close to the entrance. Momentum exchange occurs between the solid–liquid two phases, resulting in a large velocity gradient in the transverse direction on the Z section and obvious velocity inhomogeneity on the Z section.
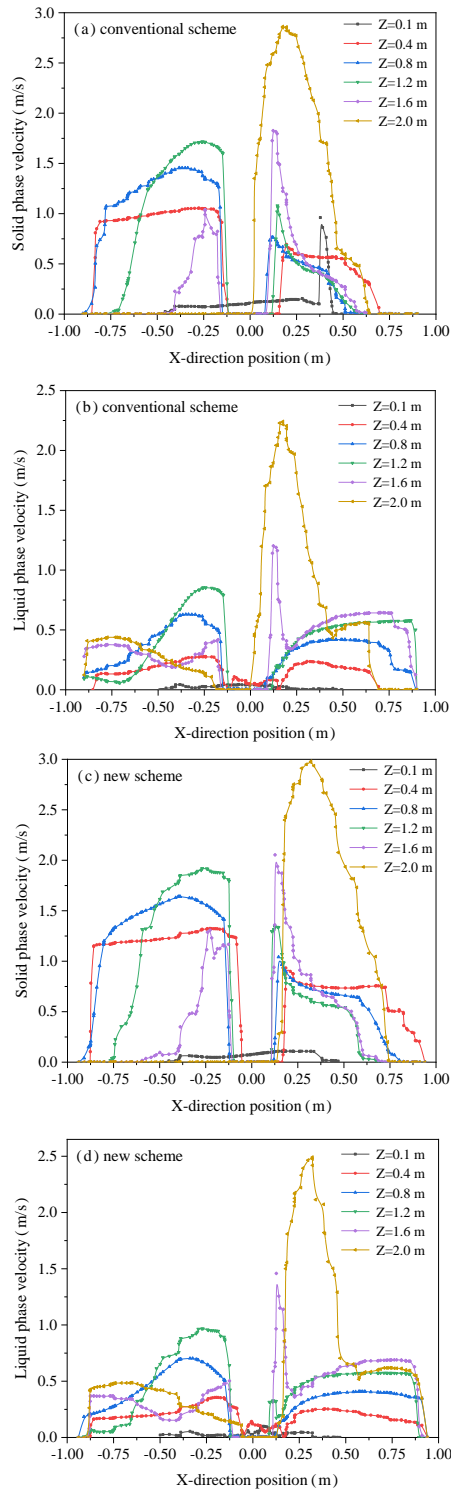
As the fluid continues to deposit downward, its velocity decreases from 2.2 m/s at the top to 0.2 m/s. When the motion of the mixed fluid is close to the low end area of the intermediate warehouse, the velocity distribution on the same Z section is relatively uniform, and the flow tends to be stable. This condition is because in the first half of the movement, the slurry fluid has lost most of its energy. The fluid micelles near the low end of the intermediate warehouse are in a state of force close to equilibrium under the combined action of gravity, inertial force, viscous force, resistance, and other forces. It no longer produces large lateral disturbances to the fluid around it.

The velocity distribution of the X-direction section in Fig. 7 show that the flow of slurry injected into the intermediate warehouse is approximately symmetrical along the central axis of the intermediate warehouse, and the velocity distribution forms a hat-shaped structure with a narrow upper end and a wide lower end from top to bottom.

The calculation results of Figs. 7(a) and 7(b) are compared. The velocity gradient of the fluid in the Z direction is smaller during the slurry injection process after adding the injection holes in the new scheme compared with the conventional scheme. This condition is because after the injection holes are added, the back pressure in the silo is small, the fluid flows smoothly, and the energy loss is small during the slurry injection process.

The liquid and solid phases on the intersection of the Z section and the *Y*=0 m section shown in Fig. 8 are taken as the research objects to further quantitatively analyze the velocity distribution characteristics of the solid–liquid two-phase in the intermediate warehouse. Curve fitting is performed after extracting the motion speed data of the solid–liquid two-phase, and the calculation result is shown in Fig. 8 (the speed plumb is positive when it is up, and it is negative when it is down).

Fig. 8. Liquid and solid phase velocity distributions at different cross sectional locations.

The calculation results in Fig. 8 show that the magnitude of the solid phase velocity and the change trend of the liquid phase velocity tend to be consistent in the range of −0.9–0.45 m in the X direction. However, the velocity of the liquid phase is significantly lower than that of the solid phase at the same position, indicating that a velocity slip

occurs between the phases, and the solid phase moves ahead of the liquid phase.

In the range of 0.6 m to 0.9 m in the X direction, the solid phase and liquid phase velocities are relatively different. At this time, the liquid phase velocity is much greater than the solid phase velocity. This condition is because after the slurry is injected into the intermediate warehouse at a certain angle, the dynamic pressure of the two-phase flow is small, and the resistance is small due to the low solid phase concentration in the intermediate warehouse. The solid phase particles are rapidly deposited to the lower end of the left side of the intermediate warehouse with an approximate parabolic trajectory and rarely flow toward the rear end of the slurry inlet.

Comprehensive analysis of the calculation results in Fig. 7 shows that the solid phase velocity in the intermediate warehouse is concentrated in the X-direction range of −0.5 m to 0.5 m, and the solid phase velocity near the bin wall is approximately zero. In the central area of the intermediate warehouse, a convex and concave solid phase velocity envelope can be drawn. Affected by the feed flow rate, the center of the velocity envelope tends to shift to the right. At the same time, the closer to the bottom of the intermediate warehouse, the smaller the absolute value of the velocity on the Z section, and the smaller the fluctuation of the two-phase flow on the same section. This condition shows that during the flow of the ore slurry from top to bottom, the flow velocity is significantly attenuated. When it reaches the bottom of the intermediate warehouse, the velocity fluctuation has minimal disturbance to the bottom fluid, which is conducive to the smooth settlement of the ore particles.
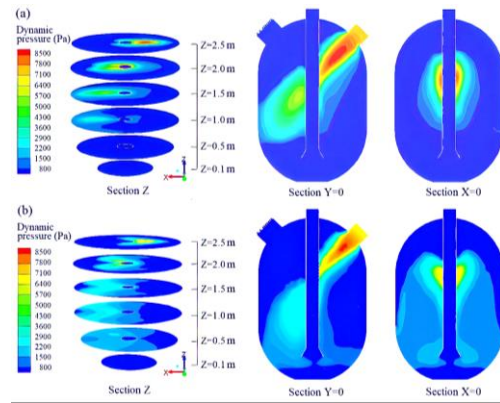
Compared with the conventional scheme, the solid phase and liquid phase velocities, and the fluid movement velocity in the new scheme are significantly larger. This condition is also the reason why the slurry injection process in the new solution operates more efficiently.

4.3 Pressure Field Distribution

Figure 9 shows the cloud map of dynamic pressure distribution at different sections. Figure 9(a) displays the calculation result of the new scheme, and Fig. 9(b) indicates the calculation result of the conventional scheme. The cloud diagram of the dynamic pressure distribution of the Z section shows that the dynamic pressure in the intermediate warehouse radiates from the top to the bottom from the center to the surrounding during feeding. The closer to the pulp inlet, the more concentrated the dynamic pressure, and the more uneven the pressure distribution at the same section. The closer to the lower end of the intermediate warehouse, the more dispersed the dynamic pressure, and the smaller the lateral pressure fluctuation at the same section.

From the *Y*=0 section pressure distribution, the dynamic pressure diffusion area is mainly concentrated in the right rear of the jet channel. It is beneficial to drive the original liquid-phase seawater in the intermediate warehouse to rotate in the counterclockwise direction in the intermediate

Fig. 9. Cloud map of dynamic pressure distribution at different sections.

pressure fluctuation in the intermediate warehouse is the main reason for the flow instability.

warehouse and then squeeze it to flow from the seawater overflow to the external marine environment. From the *X*=0 section pressure distribution, the dynamic pressure in the X direction is approximately symmetrically distributed along the axis of the lifting hard tube, and the dynamic pressure core area has an approximately elliptical structure on the *X*=0 section.
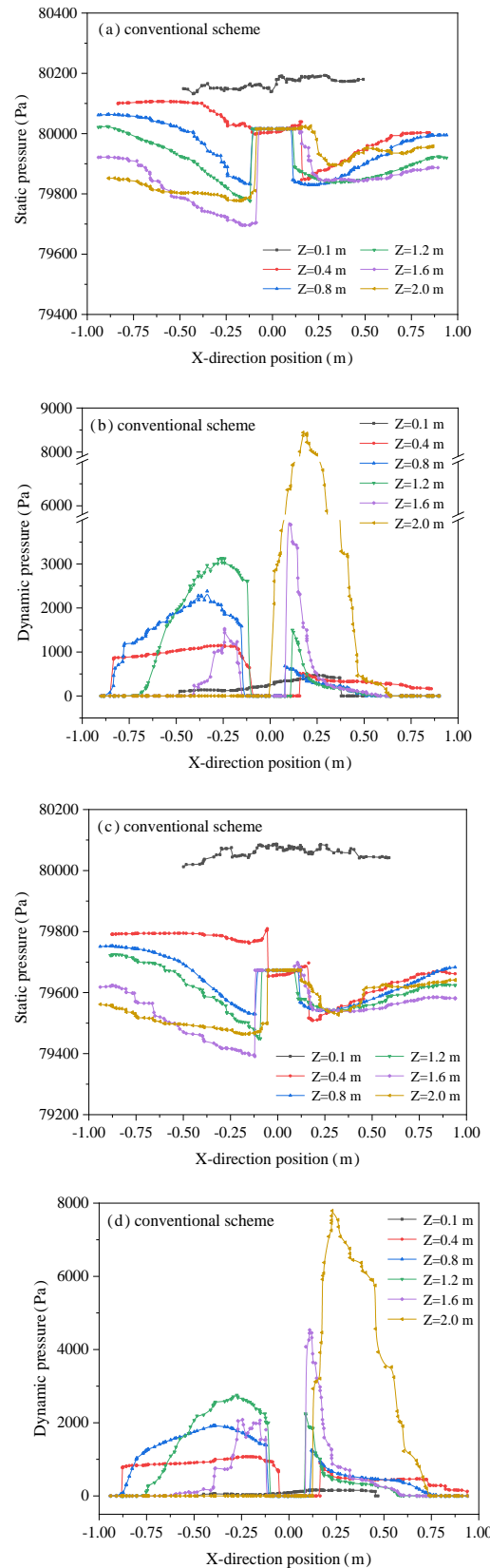
The data of static pressure and dynamic pressure on the intersection of different Z sections and *Y*=0 m sections in the intermediate warehouse are extracted to further analyze the change in pressure distribution in the flow field during the feeding process in the intermediate warehouse. Curve fitting is performed on it, and the pressure distribution curve is obtained, as shown in Fig. 10.

At different sections, from top to bottom, the static pressure continuously increases, and the difference between the two Z sections of the upper and lower layers is about 100 Pa. The fluctuation range of static pressure at the same section is small, which is mostly negligible compared with its own pressure value.

From the dynamic pressure variation laws at different X positions, the pressure fluctuations at different positions on the cross section are larger, and the variation laws of the curves tend to be consistent with the flow velocity variation laws in Fig. 8. This condition shows that the submerged jet is the main factor causing the lateral pressure fluctuation in the intermediate warehouse.

The static and dynamic pressures at different positions in the intermediate warehouse in Figs. 10(a) and 10(b) are compared. At the same section, the dynamic pressure is much smaller than the static pressure, and the difference between the two is approximately an order of magnitude. For example, the static pressure is about 80,000 Pa, and the dynamic pressure is only 1000 Pa on the section of *Z*=0.4 m. Although the absolute magnitude of dynamic pressure is much smaller than that of static pressure, its fluctuation range cannot be ignored. At the same Z section, the maximum fluctuation range of dynamic pressure is close to 8000 Pa. The dynamic pressure fluctuation range at different Z sections can reach 2000–7000 Pa. The dynamic
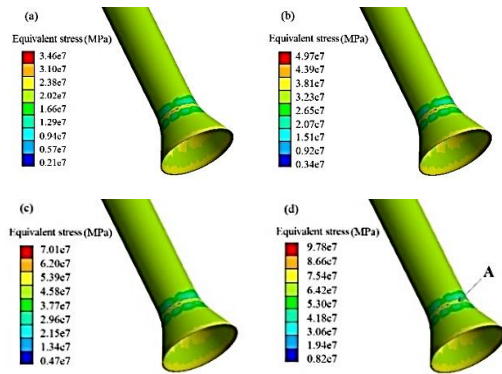
Fig. 10. Pressure distribution curve.

4.4 Fluid–Solid Coupling Analysis of Slurry Injection Process

During the slurry injection process, the mechanical effect of the internal flow field on the hard tube must be studied to prevent the early stress damage of the hard tube. On the basis of the above finite element analysis model, this study defines the wall of the hard tube as the fluid–structure interaction interface and then applies the fluid load to the hard tube. The fluid–structure interaction mechanical behavior of the hard tube under different influencing factors is analyzed. The material properties of the hard tube are shown in Table 8.

Table 8 Material properties of the hard tube

Para-m-eter	Inner diam eter (mm)	Outer diam eter (mm)	Dens ity (kg/m^3)	Elasti c Modu lus (GPa)	Poiss on's ratio
Valu e	200	210	7850	210	0.3

Figure 11 shows the cloud map of stress distribution of the lifting hard tube in the intermediate warehouse when the feed flow rate is 180, 220, 260, and 300 m^3/h, the maximum stress of the lifting hard tube increases gradually with the increase in the feed flow rate.
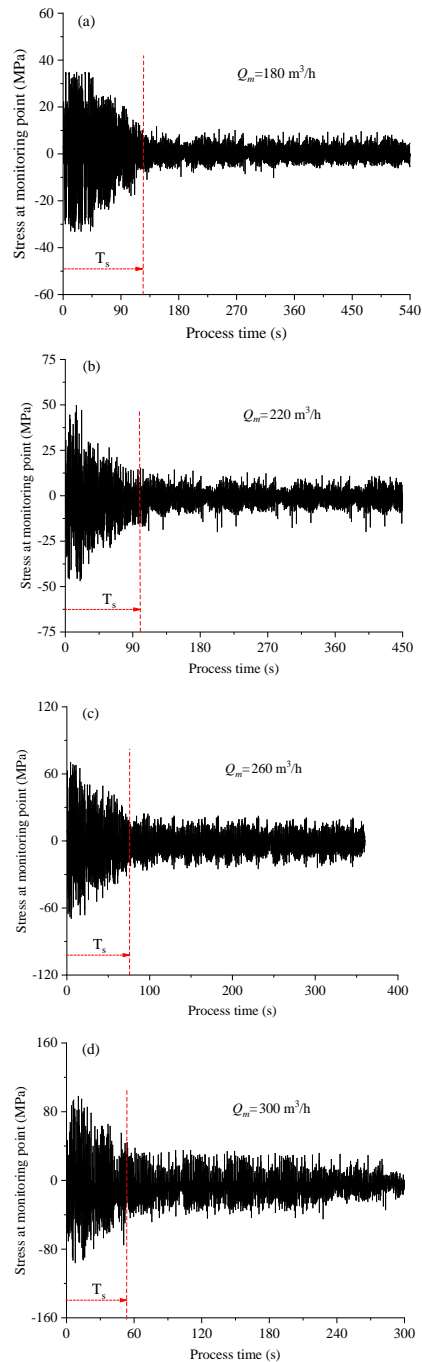

Fig. 11. Stress cloud map of hard tube fluid–structure interaction.

The maximum stress point occurs at the connection between the cylindrical section of the lifting tube and the bell mouth. The maximum stress is only 34.6 MPa when the feed flow is 180 m^3/h, and the maximum stress increases to 97.8 MPa when the feed flow is 300 m^3/h. The size of the feed flow has a great influence on the force of the lifting hard tube in the intermediate warehouse.

The stress state of the stress extreme point (point A) was monitored during the calculation process to further study the stress variation law of the stress extreme point in the feeding process. Under different feed flow rates, the stress change curve at point A during the feed cycle is shown in Fig. 12.

Fig. 12. Stress change curve of monitoring point.

The calculation results show that the overall trend of the stress change at monitoring point A tends to be consistent when the feed flow rate is different. They all increase first and then gradually decay to a steady state. This condition is because at the initial stage of feeding, the probability of the ore impacting the hoisting hard tube increases with the increase in the ore concentration in the intermediate warehouse, resulting in an increase in the local stress of the hoisting hard tube. The ore starts to accumulate at the

bottom of the intermediate warehouse after feeding for a period of time. When the ore accumulation height reaches the bell mouth at the lower end of the lifting pipe, the ore has a limited position on the bell mouth, which limits the lateral swing of the bell mouth. Therefore, the stress amplitude at the connection between the bell mouth and the lifting pipe begins to decrease. When the ore continues to accumulate, the stress amplitude of monitoring point A tends to be stable, and the fluctuation amplitude is small.

The time required for the stress amplitude of monitoring point A to change from large to small until it tends to be stable is defined as the decay period, which is represented by *Ts*. The calculation results in Fig. 13 show that the stress amplitude decay periods are 120, 100, 75, and 50 s when the feed flow rates are 180, 220, 260, and 300 m^3/h, respectively. This condition is because the greater the feed flow rate, the greater the rate of ore accumulation. When the ore stacking height exceeds the position of the bell mouth, it limits the lateral bending of the bell mouth, so the stress amplitude of the monitoring point A decreases accordingly. At the same time, the larger the feed flow rate, the larger the steady-state stress amplitude. This condition is because the greater the feed flow rate, the greater the energy of the pulp impacting the intermediate warehouse, which causes the intermediate warehouse to swing slightly laterally in the deep sea environment, and the overall stress amplitude of the lifting hard tube increases accordingly. Therefore, the feeding flow rate should not be extremely large when the feeding time is met.

5. CONCLUSION

In this study, the mathematical model and mechanical analysis model of the ore transmission process in the intermediate warehouse are established by using the proposed intermediate warehouse of a new type of ore conveying equipment. Numerical calculation and experimental research are performed on the working process of ore injection into the intermediate warehouse by using the calculation method provided by computational fluid dynamics. The conclusions are summarized as follows:

(1) The larger the slurry conveying flow, the shorter the time required for ore conveying. During the grouting process, the mixed fluid gradually spreads from the center of the intermediate warehouse wall to the surrounding. The closer to the inlet, the more uneven the velocity distribution on the Z section. The fluid velocity in the middle region is significantly higher than that of the peripheral fluid.

(2) In the range of 0.6 m to 0.9 m in the X direction, the solid phase and liquid phase velocities are relatively different. A velocity slip occurs between the phases, and the solid phase moves ahead of the liquid phase. The closer to the pulp inlet, the more concentrated the dynamic pressure, and the more uneven the pressure distribution at the same section. The closer to the lower end of the intermediate

warehouse, the more dispersed the dynamic pressure, the smaller the lateral pressure fluctuation at the same section. The dynamic pressure fluctuation in the intermediate warehouse is the main reason for the flow instability.

(3) With the impact of ore during the feeding process, the maximum stress point occurs at the connection between the cylindrical section of the lifting tube and the bell mouth. The feed flow has a great influence on the force of the lifting hard tube in the intermediate warehouse. Although the maximum stress value is much smaller than the allowable value of the material, early fatigue failure should be prevented in practical work.

REFERENCES

Cheng, X. R., R. N. Li and Y. Gao (2013). Numerical research on the effects of impeller pump-out vanes on axial force in a solid-liquid screw centrifugal pump. *Iop Conference Series: Materials Science & Engineering* 33(1), 257-260.

Dasheng, T., Y. Ning, G. Dewen, X. Hong and X. Jianxin (2015). Experimental study of manganese nodules pump in deep-sea mining. *The Ocean Engineering* 33(04), 101-107.

Felippa, C. A. and J. S. Chung (1981). Nonlinear Static Analysis of Deep Ocean Mining Pipe-Part I: Modeling and Formulation. *Journal of Energy Resources Technology* 103(1), 11-15.

Gazis, I. Z., T. Schoening and E. Alevizos (2018). Quantitative mapping and predictive modeling of Mn nodules' distribution from hydroacoustic and optical AUV data linked by random forests machine learning. *Biogeosciences* 15(23), 7347-7377.

Grebe, H. (1997). *General mathematical model for strand connections between mobile deep-sea equipment and their parent stations*. University of Siegen, Siegen, Germany.

Hailiang, X. (2008). Research on the pump－vessel combined ore lifting equipment for deep-sea rigid pipe mining system. *Journal of Offshore Mechanics & Arctic Engineering* 130(1), 244-254.

Hai-Liang, X., Chen, W. and C. Xu (2019). Cavitation performance of multistage slurry

pump in deep-sea mining. *AIP Advances* 9, 105024.

Hailiang, X., C. Wei and H. Wengang (2020). Hydraulic transport flow law of natural gas hydrate pipeline under marine dynamic environment. *Engineering Applications of Computational Fluid Mechanics* (14)1, 507-521.

Hoffmann, E. O. (1995). *Behaviour of flexible interconnection lines between moving underwater devices and floating stations*. University of Aachen, Aachen, Germany.

Xu, H., G. Zhou, W. Wu and B. Wu (2012). Numerical calculation and analysis of solid-liquid two-phase flow in deep sea mining storage tank transportation equipment. *Journal of Central South University* 43 (1), 111-117.

Yang, F. Q., H. L. Xu, W. R. Wu and B. Wu (2011). Geometric nonlinear static force analysis on the flexible mineral transporting pipe for sea mining. *Proceedings of the 4rd ICMEM International Conference on Mechanical Engineering and Mechanics*. August 11-12, Suzhou, P. R. China, p469-493.